Heat and Mass Transfer (2020) 56:913–930
https://doi.org/10.1007/s00231-019-02755-2

ORIGINAL

Performance investigation of a solar thermal collector provided with air jets impingement on multi V-shaped protrusion ribs absorber plate

Raj Kumar[1] · Rahul Nadda[2] · Adit Rana[1] · Ranchan Chauhan[3] · S. S. Chandel[1]

Received: 23 April 2019 / Accepted: 25 September 2019 / Published online: 5 November 2019

Abstract

In the present work, the heat transfer through a solar thermal collector (STC) provided with jet air impingement on the absorbent plate fitted with multi V-shaped protrusion ribs is investigated experimentally. The investigation is carried out for geometric parameters such as Relative width ratio (W_{PR}/W_{APR}), Relative protrusion rib height (h_{PR}/d_{PR}), Relative pitch ratio (P_{PR}/h_{PR}), Angle of attack (α_{PR}) respectively. The values of the streamwise pitch ratio (X_{SW}/d_h) = 0.40, spanwise pitch ratio (Y_{SW}/d_h) = 0.85 and jet diameter ratio (d_j/d_h) = 0.064 are kept constant. The overall performance of STC is effectively evaluated by varying Reynolds number (Re) in the range 2500–35,000. The results obtained from the experiments shows that the impingement jets flow on multi V-shaped protrusion ribs absorber plate accelerated the heat transfer through the solar collector channel. The optimal augmentation is obtained at W_{PR}/W_{APR}= 5, h_{PR}/d_{PR}= 0.9, P_{PR}/h_{PR} = 8 and α_{PR} = 65° respectively. Thermal-hydraulic performance parameter (η_{PR}) has also been investigated and the maximum value of 3.44 is obtained for the range of parameters studied.

Nomenclature and abbreviations

A_p	Surface area of the heated plate, m^2
A_o	Area of the orifice, m^2
C_d	Coefficient of discharge
C_f	Specific heat of fluid, J/kgK
d_h	Hydraulic diameter of the channel, m
d_j/d_h	Jet diameter ratio
d_j	Diameter of the jet, m
f_r	Friction factor of roughened protrusion rib
f_{ss}	Friction factor of the smooth surface
h_t	Convective heat transfer coefficient, W/m^2K
H_C	Height of the channel, m
h_{PR}	Height of the protrusion rib, m
h_{PR}/d_{PR}	Relative protrusion rib height
K_f	Thermal Conductivity of fluid, W/mK
L_t	Length of the test section, m
L_v	Length of V-shaped protrusion rib, m
m_a	Mass flow rate of fluid, kg/s
Nu	Nusselt number of rough fund surface
Nu_{ss}	Nusselt number of the surface without protrusion
P_{PR}	Pitch of protrusion rib, m
P_{PR}/h_{PR}	Relative pitch ratio
$(\Delta_p)_d$	Pressure fall across test section, Pa
$(\Delta_p)_o$	Pressure fall across orifice plate, Pa
Q_u	Useful heat achieve, W
Re	Reynolds number of flowing fluid
T_f	Average temperature of the fluid, K
T_i	Inlet temperature of the fluid, K
T_o	Outlet temperature of the fluid, K
T_p	Plate temperature of fluid, K
U	Mean fluid velocity, m/s
U_L	Overall heat loss coefficient
V	Velocity of fluid, m/s
W_{PR}/H_C	Channel aspect ratio
W_{PR}	Width of protrusion channel, m
W_{VPR}	Width of a single V-protrusion rib, m
W_{PR}/W_{APR}	Relative width ratio
X_{SW}/d_h	Streamwise variation
Y_{SW}/d_h	Spanwise variation
STC	Solar thermal collector

✉ Raj Kumar
nitutgt@gmail.com

[1] Faculty of Engineering and Technology, Shoolini University, Solan, H.P 173229, India

[2] Department of Mechanical Engineering, Indian Institute of Technology Ropar, Rupnagar, Punjab, India

[3] Department of Mechanical Engineering, Dr. B.R. Ambedkar NIT, Jalandhar 144011, India

SAC	Solar air channel
SAH	Solar air heater
THP	Thermo-hydraulic performance
Re	Reynolds Number

Greek symbols

α_{PR}	Angle of attack,°
β_R	Ratio of orifice meter to pipe diameter, No dimension
ρ_f	Density of fluid, kg/m^3
ν_a	Kinematic viscosity of fluid, m^2/s
η_{PR}	Thermo-hydraulic performance parameter

1 Introduction

The world is facing the energy crises and severe climate change that exceed the ability of usual managed human systems to acclimatize. The only solution to this difficulty is to exploit renewable energy sources where solar energy coming from the sun in the form of radiant energy is by far the mainly outstanding one [1, 2]. The solar thermal collector (STC) used ambient air as the heat carrying medium [3]. It is a prime component of the utilization of solar energy [4, 5]. Such type of solar thermal collectors requires low maintenance and having fewer prices as compared to other collectors [6–8]. The thermal performance of STC is low because of the low heat transfer coefficient between moving fluid and heated plate [9, 10]. Thermal performance can be improved either by increasing the heat transfer area or by enhancing the absorber to air convective heat transfer coefficient and can be achieved by modification in the stream passage of STC [10–12]. Nadda et al. [13] investigated *Nu* and f_r of an impingement jets SAH. They obtained the highest value of η_{PR}= 3.14 at P_{PR}/h_{PR}= 9.5, W_{PR}/W_{APR}= 5.0, h_{PR}/d_{PR}= 1.0 and α_{PR}= 55°. Chauhan et al. [14] carried out an exergy-based analysis of an impinging jet SAC. They found that exergetic efficiency of impinging jet SAC rises at smaller *Re* and increase in temperature parameter. Chauhan et al. [15] reviewed the performance enhancement techniques of an impinging jet STC based upon thermodynamic structure, *Nu* and f_r behavior and the multi-criteria option creation methods. Matheswaran et al. [16] examine the influence of different parameter m_a, X_{SW}/d_h, Y_{SW}/d_h and d_j/d_h on the exergy efficiency of a SAH. Based on the simulation consequences the augmented exergy efficiency was 4.36%. Aboghrara et al. [17] compared *Nu* and f_r of smooth jet impinging SAH with the corrugated rough funned channel. The outcome shows that the average thermal efficiencies of a rough funned SAH increase 14%. Brideau and Collins [18] developed a model for enhancement of the thermal efficiency of a collector with jets impingements. During analysis, they studied the effect of time set up and thermal mass on the reliability of the model. Chauhan et al. [19] investigated the effect of various parameter X_{SW}/d_h, Y_{SW}/d_h and d_j/d_h on *Nu* and f_r of impinging jets, SAH with *Re* varies from 3800 to 16,000. The outcome shows that there is significant augmentation in *Nu* and f_r. Guo et al. [20] analyzed *Nu* and f_r of a circular jets impingement STC. During the investigation the *Re* number was varied from 14,000 to 53,000, space among nozzle exit and plate from 4 to 8 and inner nozzle diameter was kept constant 6 mm. Nadda et al. [21] performed the experimental study on impingement jet SAH by using multiple arcs protrusion ribs and reported a THP of 3.64 for Re of 13,000. Rajaseenivasan et al. [22] incorporate a jets impingement arrangement in the SAH. They examined the effect of α_{PR}, m_a and nozzle diameter on *Nu* and f_r of SAH. The higher η_{PR} of 2.19 was achieved with m_a of 0.016 kg/s, nozzle diameter of 5 mm and α_{PR} of 30°. Nadda et al. [23] examine *Nu* and f_r of a jets impingement arc obstacle SAH. Testing was performed by varying *Re* from 4000 to 18,000, P_{PR}/h_{PR} (9 to 12), h_{PR}/d_{PR} (0.8 to 1.7), X_{SW}/d_h (0.39 to 0.56), Y_{SW}/d_h(0.82 to 0.99) and α_{PR}= 60°. They reported that the highest η_{PR} was obtained at P_{PR}/h_{PR}=10, h_{PR}/d_{PR}=1.1, X_{SW}/d_h= 0.43, Y_{SW}/d_h=0.86 and α_{PR}= 60°. Mishra et al. [24] used AHP-TOPSIS method to determine the optimum set of multi-arc protrusion ribs employed in impingement jet SAH. They found that the whole performance of impingement jet SAH was improved up to 3.64 times as compared to other SAH having a flat surface. Geers et al. [25] employed the PIV method to determine mean and fluctuation velocity constituent in a single and multiple both jet impingement streams. Kercher and Tabakoff [26] examine *Nu* of a perforated plate of a number of the square array and circular air jets impingements. During experimentation, they studied the influence of the jet used air flowing at right angles to the jets, d_j, X_{SW} and Z. The outcome shows that *Nu* rise with rising open area. Metzger et al. [27] experimentally investigated the effects of channel height and hole spacing on *Nu*. The outcomes show that considerable periodic variations obtain in the streamwise *Nu* profiles. Matheswaran et al. [16] examine the influence of m_a, X_{SW}/d_h, Y_{SW}/d_h and d_j/d_h on the η_{EXR} of a SAH. The outcomes are obtained at the optimized values of X_{SW}/d_h = 1.739, Y_{SW}/d_h = 0.869 d_j/d_h = 0.065 and m_a of 0.0035 kg/s. The calculated utmost η_{EXR} was 4.36%. Brideau et al. [28] developed a model of the collector and validated it with the outcome obtained from the prototype of the system. Model is used to compare and optimize the design of the collector. The results provided by the model were found to be reasonable. Nadda et al. [29] examine the outcomes of an impingement jet SAH. During experimentation, they analyze *Nu* and f_r. Also, PSI approach has been employed to optimize the design parameter for utmost yield. Goodro et al. [30] analyzed the influence of Mach number on *Nu*, coefficient of discharge & recovery factor for an array of impinging jets. During experimentation both Mach number and *Re* were varied. They found that the best outcomes were obtained at a Mach number of 0.74 and *Re* of 60,000. Goodro et al. [31] analyzed the influence of hole spacing on spatially-resolved *Nu* from

impinging jets on a flat plate. The parameters range were varied *Re* from 8200 to 30,500, Mach number from 0.1 to 0.6, X_{SW}/d_h and Y_{SW}/d_h both 8*D* and 12*D*. They found that at Mach numbers larger than 0.2 whereas *Re* kept constant show that Mach number has a considerable impact on overall *Nu*. For 8*D* spacing, *Nu* is increased significantly as the Mach number increases and for hole spacing of 12*D*, *Nu* also increases considerably as the Mach number increases. Lee et al. [32] examine the effect of impingement cross-streams on local, line-averaged and spatially. During testing, they varied the Z. They reported that the better outcome is obtained at hole spacing of 5*D*, Z of 1.5*D* and 3.0 *D*, X_{SW}/d_h and Y_{SW}/d_h= 5 and Z/D = 3.0. Nayak and Singh [33] compare $\eta_p$of a modified SAH with traditional SAH. They found η_p, *Nu* & exit fluid temperature of a cross-stream staggered hole jet plate SAH are considerably superior at m_a= 0.064 kg/s and *Re* = 5205 as compared to traditional SAH. Soni and Singh [34] examine the effect of *Re* , m_a, X_{SW}/d_h, $Y_{SW}/d_h$and d_j/d_h on the *Nu* and f_r of a Jet plate SAH. The stream parameter such as *Re* varied from 4600 to 12,000, X_{SW}/d_h and Y_{SW}/d_h both varied from 0.53 to 0.63 and d_j/d_h from 0.053 to 0.084. They also developed a correlation for these parameters. Yu et al. [35] numerically investigated the *Nu* characteristic of a small-air-jet impingement channel. They concluded that with the drop off of jet-to-plate distance the *Nu* close to stagnation point is improved, while it is reduced close to a boundary point. Zukowski [36] gives the use of micro jet method to improve the amount of heat transfer in their investigation. They reported in their analysis that the single glass covering considerably increase the efficiency of solar energy change from 16 to 24%.

From the above-cited literature survey, it is concluded that numerous investigations have been carried out by the different researchers with an array of impinging jets onto the heated surface in solar thermal collectors for its thermal improvement. Few types of research have been reported in the literature for an array of jets impingements in STC with artificial roughness provided on the heated plate. The present experimental analysis is an attempt to link this gap by presenting an in-depth experimental examination of impinging jets STC provided with multi V-shaped protrusion ribs type artificially roughness on the heated plate. The current study is novel in a sense that no such type of examination in earlier times has been examined on impinging jets STC with this type of roughness.

2 Experimental setup detail and range of roughness parameters

The schematic design of the indoor experimental unit is depicted in Fig. 1. It involves inlet section of 500 mm, experimentally examine a section of 1200 mm length and outlet section of 300 mm length trailed by the suction blower which was propelled by a motor having 5KW, 3-phase and 230 V. To run the air through the collector channel, the motor was adjusted at the alternate end. The m_a of the air transferring through the channel was determined by employing an orifice meter combined with the U tube manometer, which contains propyl alcohol. To regulate the m_a the regulator valves were used before and afterward the blower outlet. A 18 SWG black galvanized iron sheet used for heat transfer on the surface where the heater was placed to provide a continuous flux of 1000 W/m^2. The STC was installed in parallel and series arrangements by adding different loops of nichrome wire situated on the upper wall of examination section with rest of the portions insulated. An adjustable transformer was attached to sustain a precise voltage and current to record the current travelling through the circuit to provide a controlled uniform heat flux of 1000 W/m^2. To avoid over-heating and back heating from STC, 0.5 mm thick size mica sheet was inserted

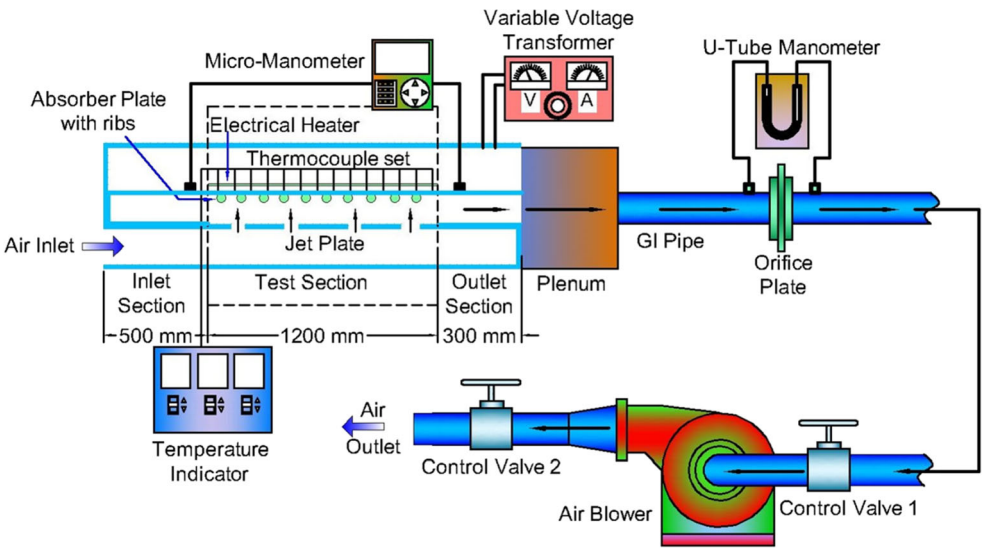

Fig. 1 Schematic design of the experimental setup

between 5 mm thick asbestos sheet and nichrome wire. The whole channel was insulated. The collector was located 30 mm above the target plate using wooden insertions. The loss of $f_r$within the testing the unit was determined by employing the micro-manometer, which estimates how much power, is required to run the air in the channel. Standardized copper thermocouples were employed to record the target plate temperature at 29 positions and were connected with quick drying thermal adhesive. Figure 2 presented the position of the variant thermocouples on the target plate. Five copper thermocouples were located at an outlet in an oblique direction and three thermocouples were located at the entry to record the temperature of the air at entry and exit respectively. The entire 29 thermocouples were connected to a temperature scanner unit to show the scanned temperature. The rectangular channel was designed so precisely so that the impinging jet plate is significantly located at its position. Figure 3 depicts the position of X_{SW}/d_h and Y_{SW}/d_hon the impingement jet plate. The deviation in the impinging jet plate alternatives and the flow *Re* for optimization of the parameters are shown in Table 1. These geometric parameters had been well optimized to achieve optimal results, which offer the highest value of *Nu* and lesser value of f_r inside the impingement jet STC.

3 Impingement jets hydrodynamics

Generally, the imposing jet is turbulent on the nozzle's outlet and is identified as a constant velocity shape. However, by raising distance from the outlet, momentum interchange among impinging jet and the ambient generates the potential core and unrestricted boundary of the jet to expand. At the downward flow of the potential core, the velocity shape is not constant above the complete jet area and a maximum of the middle velocity reduces with raising space from the outlet of the nozzle. The part of the stream on which the situations are unaffected by impinging the surface is known as free jet. In the stagnation area, the stream is affected by the surface of impulse and normally slows down and becomes hastened in the normal and crossword direction. However, the current continues to meet the zero momentum fluid from the ambient environment, crosswise acceleration in the stagnation zone in the wall jet cannot be quite stable. The shapes of velocity in the wall impinging jet are identified by nil velocity at the corresponding impingement and free plane, therefore m_a takes place in both the impinging wall jet stagnation zone. For multiple impinging jets, the stream field is affected by two types of interfaces which are not in the case of single impingement jets. The multi impingement jets stream shape can be categorized into six descriptions section: impingement section, wall jet section and free jet section, jet up wash section, jet origination section and entrainment. Because of the turbulence caused by the shear among the wall jet section and the proximal fluid, the voltage section shows the maximum heat transmission which is transferred to the edges layer in the heat convey plane. Roughened multi V-shaped protrusion ribs absorber plates with different values of W_{PR}/W_{APR} on which the fluid strikes after the impingement is shown in Fig. 4. While compared to the conventional convection cooling by the comparable restricted flow of the smooth surface, the impinging jets generate heat transfer coefficient which are three times greater due to the thin impinging jet boundary layers.

4 Data reduction

Composed data has been used to calculate h_t, *Nu* and f_r. The following are the expressions used for calculation of h_t, *Nu*, f_r and other parameters.

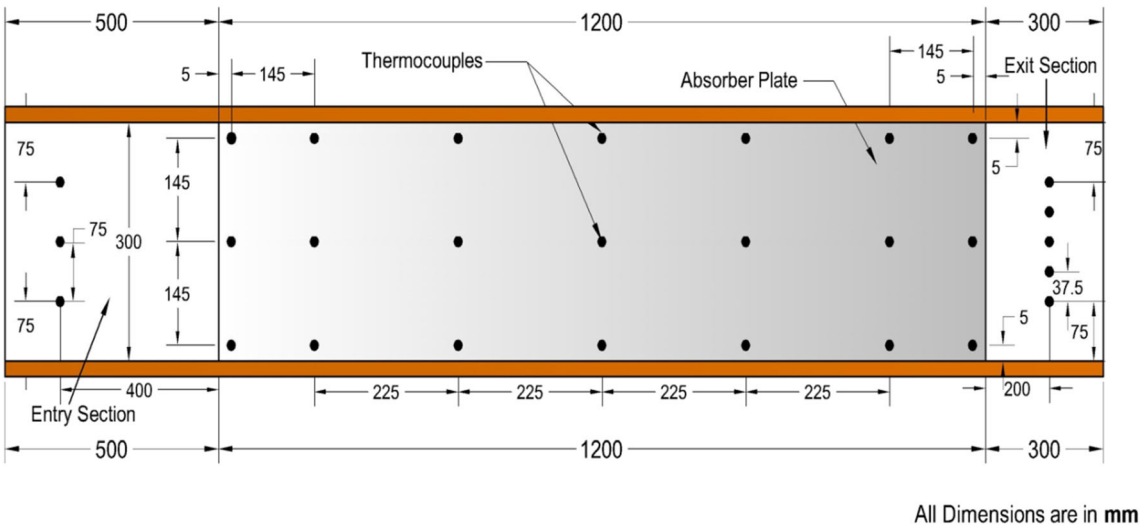

Fig. 2 Position of thermocouples on the target plate

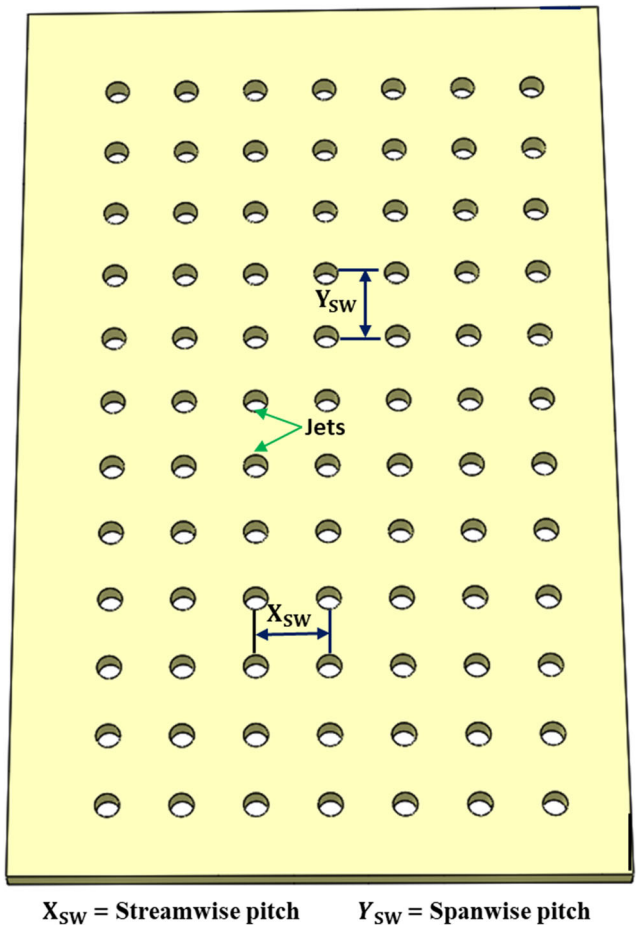

Fig. 3 Schematic design of spanwise and streamwise pitch on impingement jet plate

Temperature measured

Weighted average plate air temperature:

The average temperature of the tested plate is the average of all the temperatures of the tested plate:

$$T_p = \frac{\sum T_{pi}}{N} \tag{1}$$

Table 1 Range of variant parameters used in experimental investigation

Sr.No.	Parameters	Symbols	Range
1.	Reynolds number	*Re*	2500–35,000
2.	Relative width ratio	(W_{PR}/W_{APR})	1–6
3.	Relative protrusion rib height	(h_{PR}/d_{PR})	0.7–1.3
4.	Relative pitch ratio	(P_{PR}/h_{PR})	7–10
5.	Angle of attack	(α_{PR})	45°-85°
6.	Streamwise pitch ratio	(X_{SW}/d_h)	0.40
7.	Spanwise pitch ratio	(Y_{SW}/d_h)	0.85
8.	Jet diameter ratio	(d_j/d_h)	0.064

The average air temperature is an arithmetic mean of the entrance and exit temperature flowing through the test section:

$$T_f = \frac{T_i + T_o}{2} \tag{2}$$

Here, $T_o = (T_{A2} + T_{A3} + T_{A4} + T_{A5} + T_{A6})/5$ and $T_i = T_{A1}$

Mass stream rate measurement (m_a)

m_a has been calculated from the $(\Delta p)_0$ by using the following formula:

$$m_a = C_{do}A_o\left[\frac{2\rho_a(\Delta p)_0}{1-\beta_R{}^4}\right]^{0.5} \tag{3}$$

Velocity of air through the channel (V)

The velocity of air (V) is calculated from the $m_a$and given below

$$V = \frac{m_a}{\rho_a W_{PR} H_C} \tag{4}$$

Equivalent hydraulic diameter (d_h)

The hydraulic diameter (d_h) is calculated by using the equation given below

$$d_h = \frac{4.(W_{PR}.H_C)}{2.(W_{PR} + H_C)} \tag{5}$$

Reynolds number (*Re*)

Re of the air stream in the channel is determined by using equation as given below

$$Re = \frac{V.d_h}{\nu_a} \tag{6}$$

Friction factor (f_r)

The f_r is calculated from the measured value of $(\Delta_p)_d$ using the Darcy equation as

$$f_r = \frac{2(\Delta_p)_d d_h}{4\rho_a L_t V^2} \tag{7}$$

Heat Transfer Coefficient (Q_u)

Q_u from the absorber to the air is given by

$$Q_u = m_a c_p (T_0 - T_i) \tag{8}$$

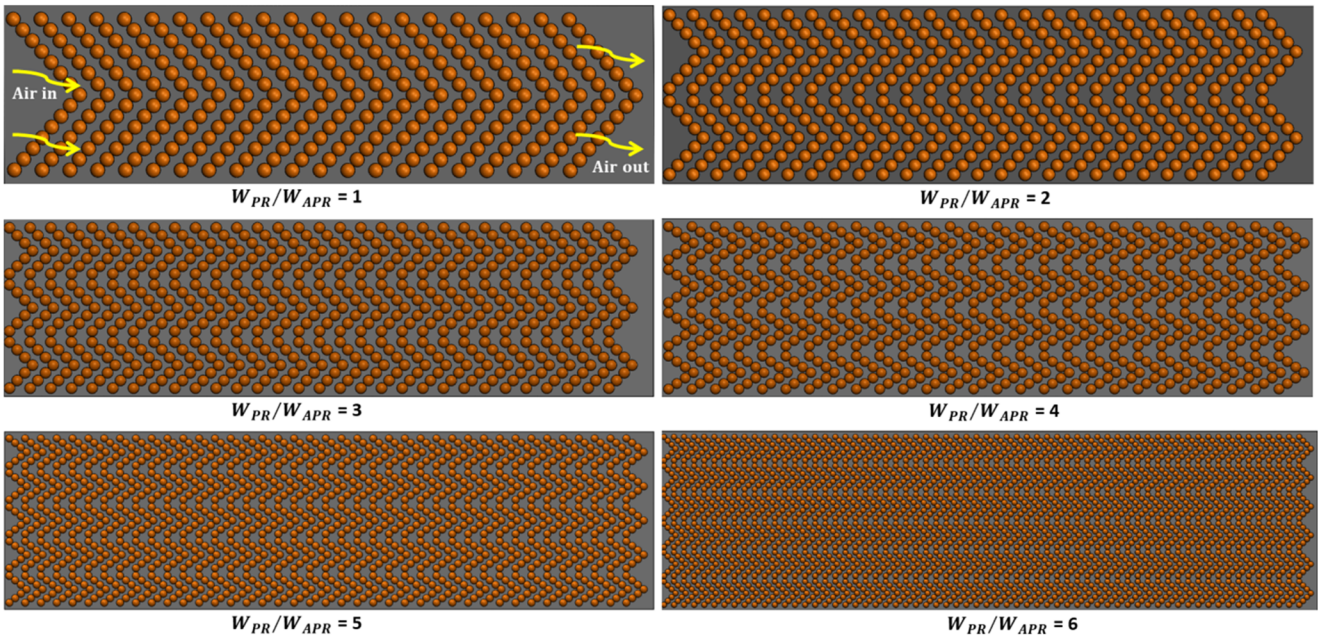

Fig. 4 Roughened multi V-shaped protrusion ribs absorber plates with different values of W_{PR}/W_{APR}

The h_t for the heated test, the section has been calculated from

$$h_t = \frac{Q_u}{A_p\left(T_p - T_f\right)} \tag{9}$$

Nusselt Number **(*Nu*)**

The h_t is used to determine the *Nu* which is given by

$$Nu = \frac{h_t d_h}{K_a} \tag{10}$$

5 Validation and uncertainty study

While executing any experiment on setup, it is necessary to confirm that the structure is giving the same response as per the previous check. Therefore, a validation inspection is done for the smooth absorber plate on the investigation system. The results obtained from the method are estimated by the reactions of the first established correlations for the rectangular channel and respectively determined by employing Eq. (11) for Nu_{ss} and Blasius Eq. (12) for f_{ss} respectively. The Nu_{ss} for smooth absorber plate in a rectangular channel is determined with Dittus – Boelter eq. as shown in Eq. (11) [37].

$$Nu_{ss} = 0.023 \times Re^{0.8} \times Pr^{0.4} \tag{11}$$

The f_{ss} for smooth absorber plate in a rectangular channel is determined by using Blasius eq. as shown in Eq. (12)

$$f_{ss} = 0.085 \times Re^{-0.25} \tag{12}$$

The estimation of experimental and predicted responses of Nu_{ss} and f_{ss} as a function of *Re* is depicted in Fig. 5a, b respectively.

Alternatively, the uncertainty analysis of measured values has been determined and is found in controlled constraints. The analysis of uncertainty for various types of operating options is given below:

6 Uncertainty study

Due to the presence of random errors, experimental results can vary from its actual results. There is a possible ratio of uncertainty error. Therefore it is important to describe the uncertainty in calibration and to estimate how these certain uncertainties increase in the analyzed outcomes [38]. The uncertainty intervals of various measurements are depicted in Table 2 and equations employed to calculate uncertainty data are given below:

Uncertainty in the measurement of A_p

$$\begin{aligned} A_p &= W_{PR} \times L_t \\ \frac{\delta A_p}{A_p} &= \left[\left(\frac{\delta L_t}{L_t}\right)^2 + \left(\frac{\delta W_{PR}}{W_{PR}}\right)^2\right]^{0.5} \\ \frac{\delta A_p}{A_p} &= \left[\left(\frac{0.1}{1200}\right)^2 + \left(\frac{0.1}{300}\right)^2\right]^{0.5} \\ \frac{\delta A_p}{A_p} &= 0.00034359 \end{aligned} \tag{13}$$

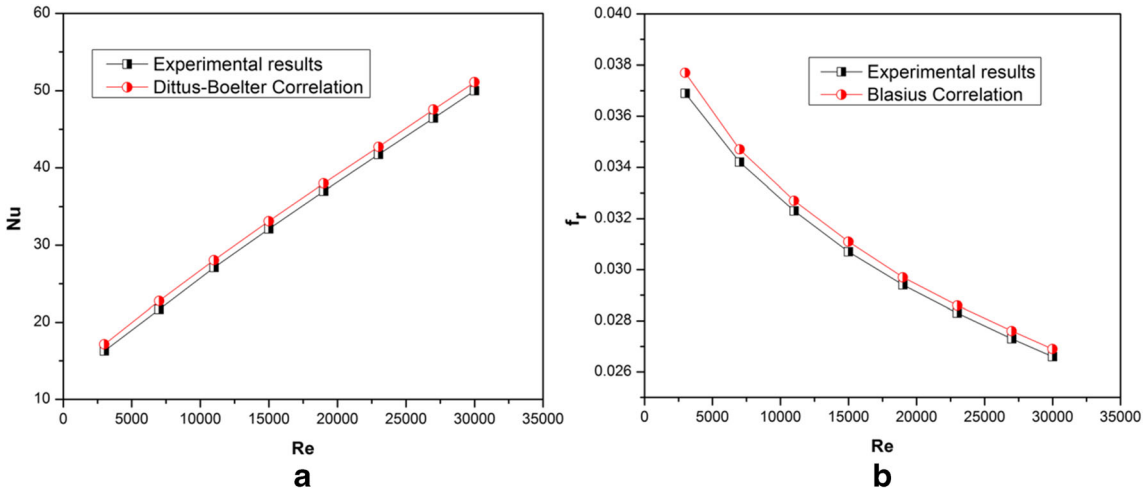

Fig. 5 **a** Comparison of expected and experimental results of Nu_{ss} **b** Comparison of expected and experimental results of f_{ss}

Uncertainty in the measurement of A_f

$$A_f = W_{PR} \times H_C$$

$$\frac{\delta A_f}{A_f} = \left[\left(\frac{\delta H_C}{H_C}\right)^2 + \left(\frac{\delta W_{PR}}{W_{PR}}\right)^2\right]^{0.5}$$

$$\frac{\delta A_f}{A_f} = \left[\left(\frac{0.1}{30}\right)^2 + \left(\frac{0.1}{300}\right)^2\right]^{0.5} \tag{14}$$

$$\frac{\delta A_f}{A_f} = 0.00334995$$

Uncertainty in the measurement of d_h

$$d_h = \frac{4 \times (W_{PR} \times H_C)}{2 \times (W_{PR} \times H_C)} = 2(W_{PR}H_C)(W_{PR} + H_C)^{-2}$$

$$\frac{\delta d_h}{\delta H_C} = \left[2(W_{PR}H_C)(-1)(W_{PR} + H_C)^{-2}\right] + \left[(W_{PR} + H_C)^{-1}(2W_{PR})\right]$$

$$\frac{\delta d_h}{\delta H_C} = \frac{2W_{PR}}{(W_{PR} + H_C)} - \frac{2W_{PR}H_C}{(W_{PR} + H_C)^2}$$

$$\frac{\delta d_h}{\delta H_C} = \frac{2 \times 300}{(300 + 30)} - \frac{2 \times 300 \times 30}{(300 + 30)^2} = 1.65289$$

$$\delta d_h = \left[\left(\frac{\delta d_h}{\delta W_{PR}}\delta W_{PR}\right)^2 + \left(\frac{\delta d_h}{\delta H_C}\delta H_C\right)^2\right]^{0.5} \tag{15}$$

$$\frac{\delta d_h}{d_h} = \frac{\left[\left(\frac{\delta d_h}{\delta W_{PR}}\delta W_{PR}\right)^2 + \left(\frac{\delta d_h}{\delta H_C}\delta H_C\right)^2\right]^{0.5}}{2(W_{PR} \times H_C)(W_{PR} + H_C)^{-1}}$$

$$\frac{\delta d_h}{d_h} = \frac{\left[(1.65289 \times O.1)^2 + (0.0165289 \times 0.1)^2\right]^{0.5}}{2(300 \times 30)(300 + 30)^{-1}}$$

$$\frac{\delta d_h}{d_h} = 0.0030304246$$

Uncertainty in the measurement of A

$$A_o = \frac{\pi}{4} D_o{}^2$$

$$\frac{A_o}{\delta D_o} = \frac{2\pi D_o}{4}$$

$$\delta A_o = \left[\left(\frac{\delta A_o}{\delta D_o}\delta D_o\right)^2\right]^{0.5} = \left[\left(\frac{\pi D_o}{2}\delta D_o\right)^2\right]^{0.5} = \frac{\pi D_o \times \delta D_o}{2} \tag{16}$$

$$\frac{A_o}{\delta A_o} = \frac{\frac{\pi D_o \times \delta D_o}{2}}{\frac{\pi}{4} D_o{}^2} = \frac{2 \times \delta D_o}{D_o} = \frac{2 \times 0.1}{42.96}$$

$$\frac{A_o}{\delta A_o} = 0.0047$$

Uncertainty in the measurement of ρ_a

$$\rho_a = \frac{P_a}{R \times T_o}$$

$$\delta\rho_a = \left[\left(\left(\frac{\delta\rho_a}{\delta P_a}\right) \times 1 \times \delta P_a\right)^2 + \left(\left(\frac{\delta\rho_a}{\delta T_o}\right) \times 1 \times \delta T_o\right)^2\right]^{0.5}$$

$$\delta\rho_a = \left[\left(\left(\frac{1}{R \times T_o}\right) \times \left(\frac{\rho_a R T_o}{P_a}\right) \times \delta P_a\right)^2 + \left(\left(-\frac{P_a}{R \times T_o{}^2}\right) \times \left(\frac{\rho_a R T_o}{P_a}\right) \times \delta T_o\right)^2\right]^{0.5} \tag{17}$$

$$\frac{\delta\rho_a}{\rho_a} = \left[\left(\frac{\delta P_a}{P_a}\right)^2 + \left(\frac{\delta T_o}{T_o}\right)^2\right]^{0.5}$$

Taking $P_a = 97500\ Pa$

$$\frac{\delta\rho_a}{\rho_a} = \left[\left(\frac{0.1}{97500}\right)^2 + \left(\frac{0.1}{25.33}\right)^2\right]^{0.5} = 3.94 \times 10^{-3}$$

$m_a = C_d A_o \left[\frac{2\rho_a(\Delta p)_0}{1-\beta^4}\right]^{0.5}$ 6. Uncertainty in the measurement of m_a

$$m_a = C_d \times A_o \times \rho_a{}^{0.5} \times (\Delta p)_0{}^{0.5} \times \left[\frac{2}{1-\beta^4}\right]^{0.5}$$

$$\delta m_a = \left[\left(\frac{\delta m_a}{\delta C_d}\delta C_d\right)^2 + \left(\frac{\delta m_a}{\delta A_o}\delta A_o\right)^2 + \left(\frac{\delta m_a}{\delta \rho_a}\delta \rho_a\right)^2 + \left(\frac{\delta m_a}{\delta (\Delta p)_0}\delta (\Delta p)_0\right)^2\right]^{0.5} \tag{18}$$

$$\frac{\delta m_a}{m_a} = \left[\left(\frac{\delta C_d}{C_d}\right)^2 + \left(\frac{\delta A_o}{A_o}\right)^2 + \left(\frac{\delta \rho_a}{\rho_a}\right)^2 + \left(\frac{\delta (\Delta p)_0}{(\Delta p)_0}\right)^2\right]^{0.5}$$

The value of

$$\frac{\delta C_d}{C_d} = 1.5\%$$

The uncertainty in $(\Delta p)_0$ for U-tube manometer is 0.2 mm.

$$(\Delta p)_0 = \Delta(H)_o sin\ 30° \times sin\ 90° = 185\ \text{mm}$$

$$\frac{\delta m_a}{m_a} = \left[\left(\frac{1.5}{100}\right)^2 + (0.0047)^2 + (0.00394)^2 + \left(\frac{0.2}{185}\right)^2\right]^{0.5} = 0.016241$$

Uncertainty in the measurement of V

$$V = \frac{m_a}{\rho_a \times W_{PR} \times H_C}$$

$$\frac{\delta V}{V} = \left[\left(\frac{\delta m_a}{m_a}\right)^2 + \left(\frac{\delta \rho_a}{\rho_a}\right)^2 + \left(\frac{\delta W_{PR}}{W_{PR}}\right)^2 + \left(\frac{\delta H_C}{H_C}\right)^2\right]^{0.5} \tag{19}$$

$$\frac{\delta V}{V} = \left[(0.016241)^2 + (0.00394)^2 + \left(\frac{0.1}{300}\right)^2 + \left(\frac{0.1}{30}\right)^2\right]^{0.5} = 0.017044$$

Uncertainty in Q_u

$$Q_u = m_a c_p (T_0 - T_i) = m_a c_p \Delta T$$

$$\frac{\delta Q_u}{Q_u} = \left[\left(\frac{\delta m_a}{m_a}\right)^2 + \left(\frac{\delta c_p}{c_p}\right)^2 + \left(\frac{\delta \Delta T}{\Delta T}\right)^2\right]^{0.5} \tag{20}$$

Uncertainty in specific heat is 0.1.
So, the equation becomes

$$\frac{\delta Q_u}{Q_u} = \left[(0.016241)^2 + \left(\frac{0.1}{1006.141}\right)^2 + \left(\frac{0.1}{5.33}\right)^2\right]^{0.5} = 0.02481$$

Uncertainty in h_t

$$h_t = \frac{Q_u}{A_p \times (T_p - T_f)} = \frac{Q_u}{A_p \times \Delta T_f}$$

$$\frac{\delta h_t}{h_t} = \left[\left(\frac{\delta Q_u}{Q_u}\right)^2 + \left(\frac{\delta A_p}{A_p}\right)^2 + \left(\frac{\delta \Delta T_f}{\Delta T_f}\right)^2\right]^{0.5}$$

$$\frac{\delta h_t}{h_t} = \left[(0.02481)^2 + (0.00034359)^2 + \left(\frac{0.1}{22.66}\right)^2\right]^{0.5} = 0.0252017 \tag{21}$$

Uncertainty in the measurement of Nu

$$Nu = \frac{h_t d_h}{K_a}$$

$$\frac{\delta Nu}{Nu} = \left[\left(\frac{\delta d_h}{d_h}\right)^2 + \left(\frac{\delta h_t}{h_t}\right)^2 + \left(\frac{\delta K_a}{K_a}\right)^2\right]^{0.5}$$

$$\frac{\delta Nu}{Nu} = \left[(0.0030304246)^2 + (0.0252017)^2 + \left(\frac{0.00001}{0.02529}\right)^2\right]^{0.5} 0.0394161 \tag{22}$$

Table 2 Uncertainty intervals of various measurements

Sr. No.	Measurement	Apparatus	Uncertainty
1.	Dimensions of STC	Vernier caliper	±0.2 mm
2.	Pressure drop across the STC	Micro-manometer	±0.2 *Pa*
3.	Pressure drop across the orifice-plate	U-tube manometer	±1mm
4.	Temperature measurement	Cu-Co thermocouple	±0.1 ° *C*
5.	Orifice plate and throat diameter	Vernier caliper	±0.1 mm

Uncertainty in the measurement of Re

$$\begin{gathered} Re = \frac{V.d_h}{\nu} = \frac{\rho_a V d_h}{\mu} \\ \frac{\delta Re}{Re} = \left[\left(\frac{\delta d_h}{d_h}\right)^2 + \left(\frac{\delta V}{V}\right)^2 + \left(\frac{\delta \rho_a}{\rho_a}\right)^2 + \left(\frac{\delta \mu}{\mu}\right)^2\right]^{0.5} \\ \frac{\delta Re}{Re} = \left[(0.0030304246)^2 + (0.017044)^2 + (0.00394)^2 + \left(\frac{0.001 \times 10^{-5}}{1.87 \times 10^{-5}}\right)^2\right]^{0.5} \\ \frac{\delta Re}{Re} = 0.01776 \end{gathered} \tag{23}$$

Uncertainty in the measurement of f_r

$$\begin{gathered} f_r = \frac{2(\Delta_p)_d d_h}{4\rho_a L_t V^2} \\ \frac{\delta f_r}{f_r} = \left[\left(\frac{\delta d_h}{d_h}\right)^2 + \left(\frac{\delta V}{V}\right)^2 + \left(\frac{\delta L_t}{L_t}\right)^2 + \left(\frac{\delta \rho_a}{\rho_a}\right)^2 + \left(\frac{\delta(\Delta_p)_d}{(\Delta_p)_d}\right)^2\right]^{0.5} \\ \frac{\delta f_r}{f_r} = \left[(0.0030304246)^2 + (0.17044)^2 + \left(\frac{0.1}{1200}\right)^2 + (0.00394)^2 + \left(\frac{0.1}{56.2}\right)^2\right]^{0.5} \\ \frac{\delta f_r}{f_r} = 0.01784 \end{gathered} \tag{24}$$

Uncertainty in the measurement of η_{PR}

$$\begin{gathered} \eta_{PR} = (Nu/Nu_{ss})/(f_{rs}/f_{ss})^{0.33} \\ \frac{\delta \eta_{PR}}{\eta_{PR}} = \left[\left(\frac{\delta Nu}{Nu}\right)^2 + \left(\frac{\delta f_r}{f_r}\right)^2\right]^{0.5} \\ \frac{\delta \eta_{PR}}{\eta_{PR}} = \left[(0.0394161)^2 + (0.01784)^2\right]^{0.5} \\ \frac{\delta \eta_{PR}}{\eta_{PR}} = 0.043265 = 4.3265\% \end{gathered} \tag{25}$$

The single test run was conducted for uncertainty analysis. Uncertainty was analyzed for a complete test run for single geometry and outcomes are offered in Table 3.

7 Results and discussion

The *Nu* and f_r characteristics of the STC are explained below with multi V-shaped protrusion ribs attached on the heated plate and tested data are collected for distinct types of geometrical factors such as W_{PR}/W_{APR}, h_{PR}/d_{PR}, P_{PR}/h_{PR} and α_{PR} .

Table 3 Range of uncertainty (for measurement of necessary parameters)

Sr. No.	Parameters	Error range %
1.	m_a	1.468–2.043
2.	V	1.543–1.821
3.	Q_u	2.233–3.269
4.	h_t	2.623–3.722
5.	Nu	3.468–4.557
6.	f_r	1.273–2.431
7.	η_{PR}	3.845–5.241

7.1 Heat transfer

In STC, the influence of W_{PR}/W_{APR} on the Nu in the stream of air-fluid is presented. The plots for Nu as a function of W_{PR}/W_{APR} for the data of Re has been presented in Fig. 6a and the remaining geometrical factors like $h_{PR}/d_{PR} = 0.9$, $P_{PR}/h_{PR} = 8$, $\alpha_{PR} = 65^{o}$, $X_{sw}/d_h = 0.40$, $Y_{sw}/d_h = 0.85$ and $d_j/d_h = 0.064$ were kept constant. It has been observed that Nu rises with a rise in W_{PR}/W_{APR} from 1 to 6 and achieves the extreme viable data correspondent to W_{PR}/W_{APR} of 5 and afterward the data of Nu begins to decrease. The graph for Nu/Nu_{ss} as a purpose of W_{PR}/W_{APR} for multi V-shaped protrusion ribs at variant selected Re is presented in Fig. 6b. It has been found that in every situation, the multi V-shaped protrusion ribs wall produces superior Nu compared to that of without multi V-shaped protrusion ribs wall. An ideal Nu is produced by the multi V-shaped protrusion ribs because multi V-shaped protrusion ribs hilltop forms a secondary flow jet. Such ensuing flow jets have the profile of two different spinning vortices which transfers the cold air fluid from the internal central portion area to the multi V-shaped protrusion ribs wall. These lower flow jets associated with the main stream. The smaller stream jets combine with the central flow generally affect the flow retraction, retransmission among the multi V-shaped protrusion ribs and downstream suspended boundary layer growth of the restriction regions. Such an upcoming flow jet shapes two different spinning vortices, which transfers the cold air fluid from the internal central part area to the multi V-shaped protrusion ribs STC wall. These lower streams are connected to the mainstream. The smaller stream jets combine with the central flow, which usually affects the flow retraction. It can be observed that after increasing the data of $W_{PR}/W_{APR} = 3$, the volume of upper and lower end also increased, which improves the secondary stream elements and gives a recognized improvement in Nu. However, Nu only improved continuously just up to a value of 5. After that as the value of W_{PR}/W_{APR} further increases the Nu decreases. The multi V-shaped protrusion ribs create a strong secondary stream jet near the limbs and when the disruption from the area of the V-shaped ribs goes out and combines with the mainstream, the disturbance conducts the turbulence mixing. It has been obtained that the extreme result for Nu is achieved at W_{PR}/W_{APR} of 5 for each data of Re.

The alteration of Nu with Re for various data of h_{PR}/d_{PR} has been shown in Fig. 7a. The rest of the geometrical parameters like $W_{PR}/W_{APR} = 5$, $P_{PR}/h_{PR} = 8$, $\alpha_{PR} = 65^{o}$, $X_{sw}/d_h = 0.40$, $Y_{sw}/d_h = 0.85$ and $d_j/d_h = 0.064$ were kept constant. It has been observed that due to expanding flow every value of Nu increases with the increase in value of h_{PR}/d_{PR} for each value of Re, which causes the maximum turbulence and result in an enhancement in Nu. The highest Nu was obtained at $h_{PR}/d_{PR} = 0.9$. Figure 7b shows the graph for Nu/Nu_{ss} as a function of h_{PR}/d_{PR} for a multi V-shaped protrusion ribs STC at variant selected Re. It has been found that from different values of h_{PR}/d_{PR} the Nu was ideal for $h_{PR}/d_{PR} = 0.9$ at each data of Re.

Figure 8a presents the distinction of Nu as a function of Re for alternative data of P_{PR}/h_{PR} and rest of the geometrical parameters like $W_{PR}/W_{APR} = 5$, $h_{PR}/d_{PR} = 0.9$, $\alpha_{PR} = 65^{o}$, $X_{sw}/d_h = 0.40$, $Y_{sw}/d_h = 0.85$ and $d_j/d_h = 0.064$ were reserved fixed. For every data of Re, the extreme values of Nu have been achieved at P_{PR}/h_{PR} of 8, while the smallest values of Nu

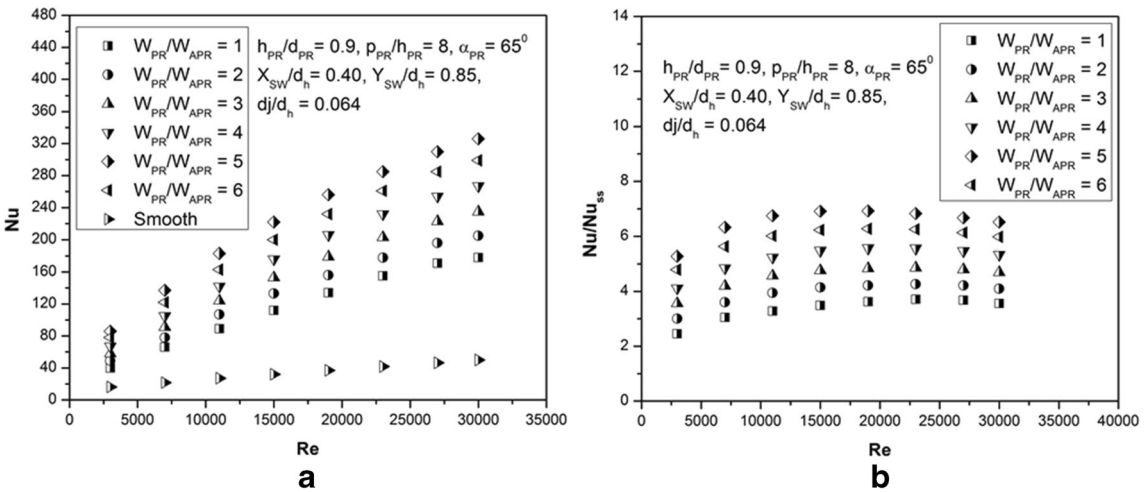

Fig. 6 **a** Effect of W_{PR}/W_{APR} on Nu **b** Effect of W_{PR}/W_{APR} on Nu/Nu_{ss} at selected Re

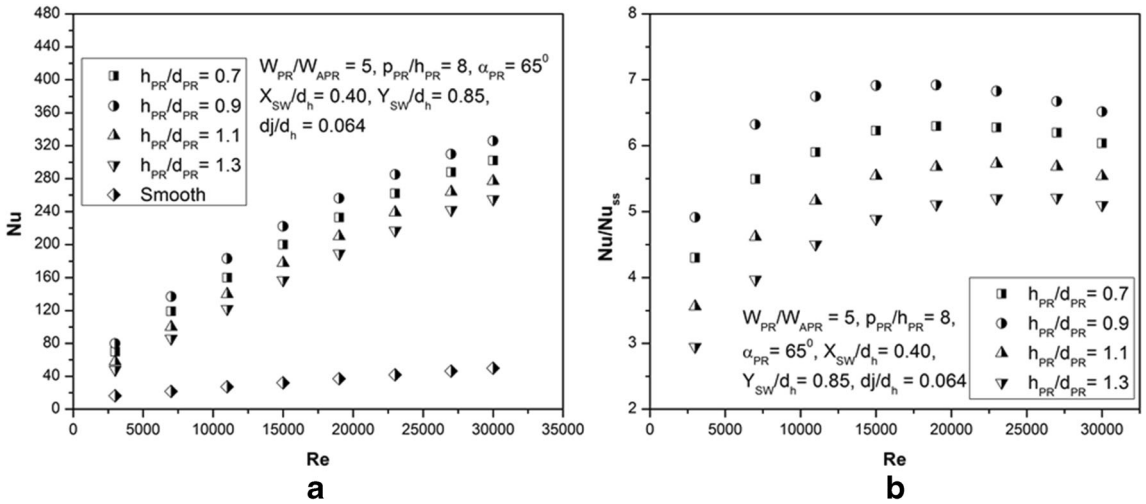

Fig. 7 **a** Effect of h_{PR}/d_{PR} on *Nu* **b** Effect of h_{PR}/d_{PR} on Nu/Nu_{ss} at selected *Re*

have been observed to increase the range of selected parameter P_{PR}/h_{PR} up to 10. This change in the results of *Nu* is due to the development of vital vortices combined with each other to eliminate the flow of V-shaped ribs and maintain the optimum value of P_{PR}/h_{PR}. Figure 8b shows the graphs for Nu/Nu_{ss} as a function of P_{PR}/h_{PR} for a multi V-shaped protrusion ribs STC at variant selected *Re*. It has been obtained from different values of P_{PR}/h_{PR} the *Nu* was highest for P_{PR}/h_{PR}= 8 at each value of *Re*.

The plot presented in Fig. 9a depicts the distinction of *Nu* with *Re* for distinctive data of α_{PR} and fixed values of the rest of the geometrical parameters like W_{PR}/W_{APR} = 5, h_{PR}/d_{PR} = 0.9, P_{PR}/h_{PR} = 8, X_{sw}/d_h = 0.40, Y_{sw}/d_h = 0.85 and d_j/d_h = 0.064 . In the above plot *Nu* has been presented as an influence of α_{PR} for entire values of *Re* and remaining constant solar air passage parameters. The *Nu* improved with the increase in α_{PR} and reaches the results consistent to 65° after that, there was a decrease in *Nu* due to an increase in the data of α_{PR}. The enhancement in α_{PR} causes a decrease in interruption of end-to-end impinging jets compared to absorber plate and hence highest *Nu* was found. Figure 9b shows the plot of Nu/Nu_{ss} for a multi V-shaped protrusion ribs STC at different selected values of *Re*. This plot depicts that at different values of α_{PR}, Nu/Nu_{ss} has been maximum for an array of 65° to entire data of *Re*.

7.2 Friction factor

The continuous implementation of roughness in the multi V-shaped protrusion ribs on the hot surface improves the effectiveness of *Nu* from the heated surface of an STC with subsequent growth in f_r losses. In the present experimental investigation, it has been proposed that how f_r characteristics of the STC were affected once multi V-shaped protrusion ribs parameters i.e. W_{PR}/W_{APR} are altered and rest of the geometrical roughness parameters like h_{PR}/d_{PR} = 0.9, P_{PR}/h_{PR} = 8, α_{PR}= 65°, X_{sw}/d_h = 0.40, Y_{sw}/d_h = 0.85 and d_j/d_h = 0.064 were kept fixed as described in Fig. 10a. The plot demonstrates that

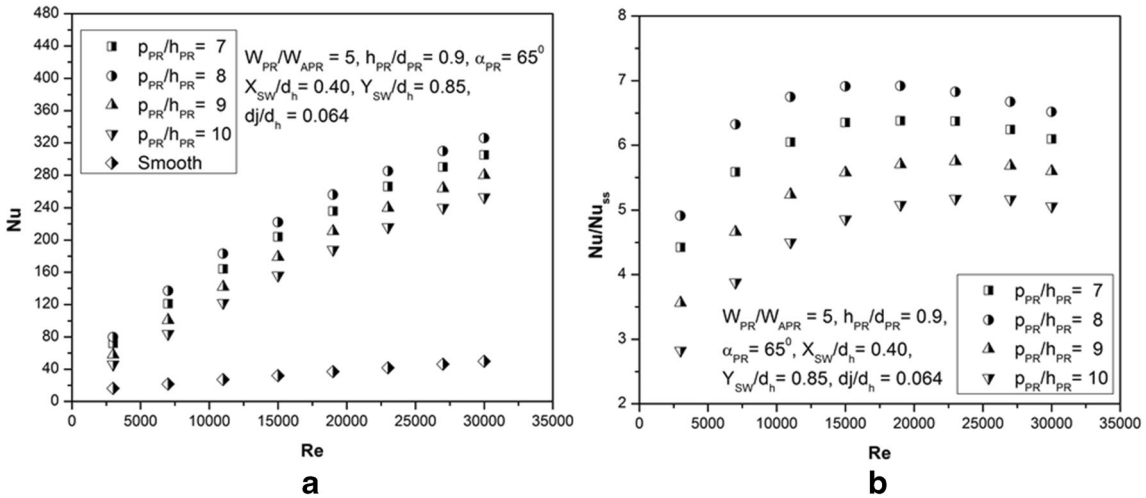

Fig. 8 **a** Effect of P_{PR}/h_{PR}on *Nu* **b** Effect of P_{PR}/h_{PR} on Nu/Nu_{ss} at selected *Re*

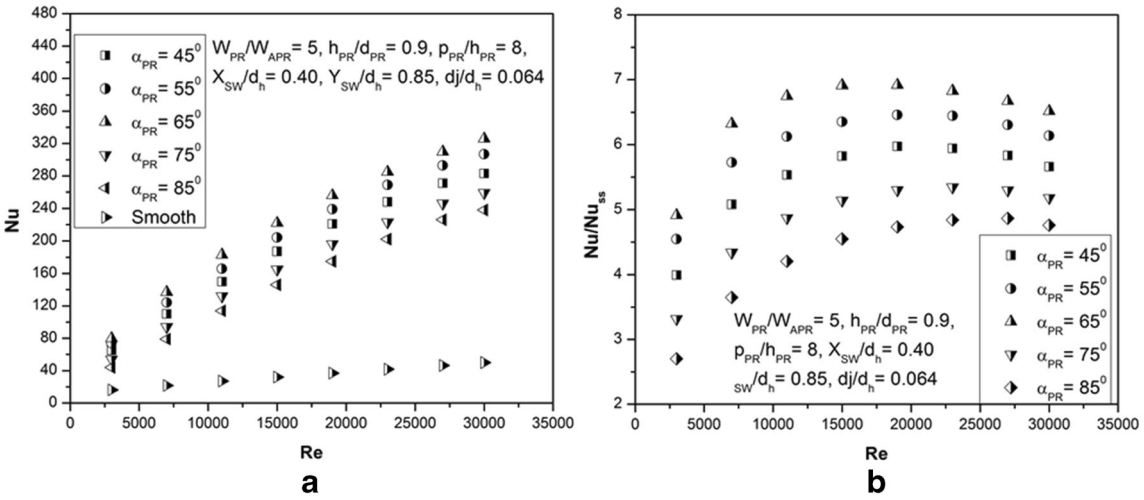

Fig. 9 **a** Effect of α_{PR} on *Nu* **b** Effect of α_{PR} on Nu/Nu_{ss} at selected *Re*

$f_r$varies with *Re* for different data of W_{PR}/W_{APR}, so due to the decrease of *Re* in each situation $f_r$was increased. From Fig. 10b it has been obtained that f_r/f_{ss} rises at values of W_{PR}/W_{APR} = 6 and the extreme value of f_r/f_{ss} has been achieved. The volume of secondary stream jets was increased in the expansion value of W_{PR}/W_{APR}. This causes an increase in the results of *Nu* up to a series of W_{PR}/W_{APR}= 5. With the rise in W_{PR}/W_{APR} the results of f_r/f_{ss} rises and achieves the highest value corresponding to W_{PR}/W_{APR} value of 6 in the range of specified parameters. Due to the partition of flow, the results of f_r/f_{ss} occurs interpretation of the structure of vortices. Some of the vortices air accumulation and this causes an increase in *Nu*. Usually, *Nu* enhances from the target plate to air and such vortices as mentioned above also improves *Nu* during the flow around the STC. The number of vortices in case of W_{PR}/W_{APR}= 6.0 was more as compared to W_{PR}/W_{APR} of 5. Therefore, for W_{PR}/W_{APR} of 6 air and vortices mixing was huge, which gives a large amount of f_r/f_{ss}.

The variance of f_r with *Re* for different data of h_{PR}/d_{PR} has been shown in Fig. 11a. The remaining roughness geometrical parameters such as W_{PR}/W_{APR} = 5.0, P_{PR}/h_{PR} = 8, α_{PR}= 65^o, X_{sw}/d_h = 0.40, Y_{sw}/d_h = 0.85 and d_j/d_h = 0.064 were kept fixed. The graph plotted for f_r in Fig. 11a proposed that for defined values of $h_{PR}/d_{PR,}$ f_r reduces with increase in *Re*. Figure 11a clearly states that f_r raises because of the increase in h_{PR}/d_{PR} and the highest value of $f_r$were obtained corresponding to h_{PR}/d_{PR} value of 0.9. Figure 11b depicts the values of f_r/f_{ss} as a meaning of h_{PR}/d_{PR} for multi V-shaped protrusion ribs STC at variant selected series of *Re*. It has been realized that at dissimilar values of $h_{PR}/d_{PR,}$the f_r/f_{ss} was maximum for h_{PR}/d_{PR}= 0.9 for respective data of *Re*. Due to the rise in the value of h_{PR}/d_{PR} the multi V-shaped protrusion ribs increase up to a large extent in the center of the stream and resulting in the growth in f_r/f_{ss} as well as turbulence fact.

Figure 12a depicts the variance of $f_r$with *Re* for different data of P_{PR}/h_{PR} and remaining of the roughness parameters

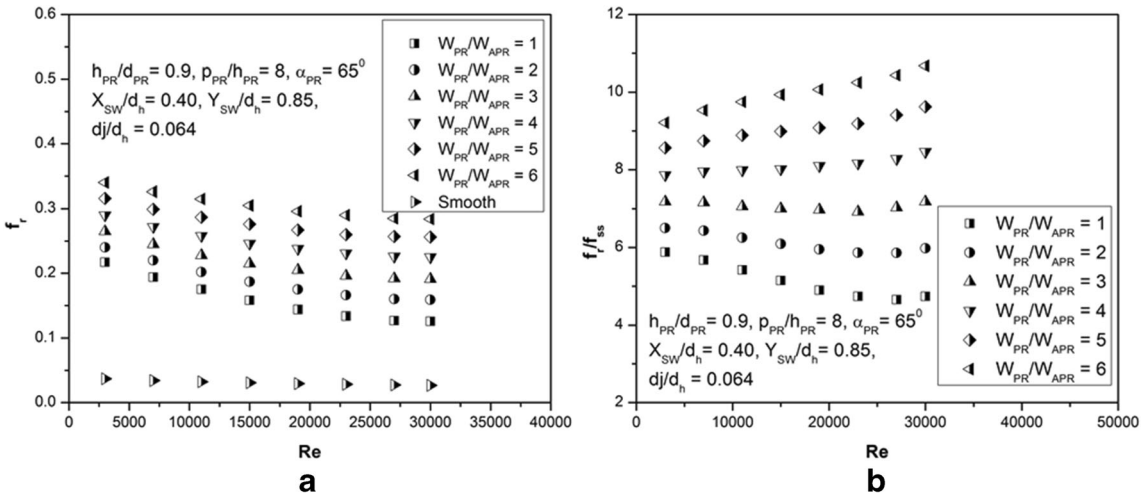

Fig. 10 **a** Effect of W_{PR}/W_{APR}on f_r **b** Effect of W_{PR}/W_{APR} on f_r/f_{ss} at selected *Re*

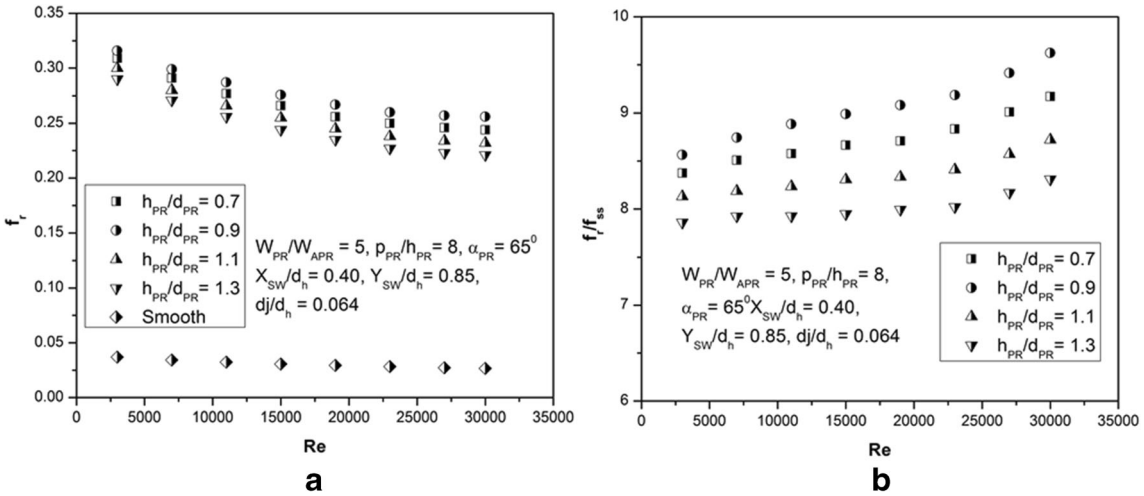

Fig. 11 **a** Effect of h_{PR}/d_{PR} on f_r **b** Effect of h_{PR}/d_{PR} on f_r/f_{ss} at selected *Re*

viz. W_{PR}/W_{APR} = 5.0, h_{PR}/d_{PR} = 0.9, α_{PR}= 65°, X_{sw}/d_h = 0.40, Y_{sw}/d_h = 0.85 and d_j/d_h = 0.064 were kept fixed. From Fig. 12a it has been found that for all value of P_{PR}/h_{PR}, f_r decreases with increase in *Re*. For P_{PR}/h_{PR} the values of 8 and 10 provides the highest and lowest value of f_r. Figure 12b represents the data of f_r/f_{ss} as a function of P_{PR}/h_{PR} for multi V-shaped protrusion ribs STC at variant arrays of *Re*. It has been found that at different values of P_{PR}/h_{PR}, f_r/f_{ss} was higher for P_{PR}/h_{PR}= 8 at respective values of *Re*.

The change of f_r with *Re* for different data of α_{PR} and remaining roughness parameters like W_{PR}/W_{APR} = 5.0, h_{PR}/d_{PR} = 0.9, P_{PR}/h_{PR} = 8, X_{sw}/d_h = 0.40, Y_{sw}/d_h = 0.85 and d_j/d_h = 0.064 which reserved steadily were shown in Fig. 13a. It has been found that for all data of α_{PR}, f_r reduces with the rise in *Re*. The plot depicts that f_r rises with a rise in α_{PR} value from 45 to 65° and later it decreases with increase in α_{PR} and receives the highest possible value correspondent to α_{PR} of 65°. The maximum and minimum values of f_r has been found at α_{PR} values of 45 and 65° respectively. Figure 13b shows the results of f_r/f_{ss} as a meaning of α_{PR} for multi V-shaped protrusion ribs, STC at variant elected arrays of *Re*. It has been found that at different values of α_{PR} the f_r/f_{ss} was highest for α_{PR}= 65°for all data of *Re*.

7.3 THP

The complete examination of *Nu* and f_r performances proposed that *Nu* in multi V-shaped protrusion ribs STC was enhanced with a significant improvement in f_r. Hence, it has been essential to select profiles which not just affect *Nu* but also resist the f_r on the lowest working stage. In order to achieve such resolution synchronized consideration of η_{PR} Lewis [39] presented a η_{PR} criterion recognized as efficiency criterion i.e. η_{PR}. Selecting the *Nu* through W_{PR}/W_{APR}, h_{PR}/d_{PR}, P_{PR}/h_{PR}, α_{PR}, X_{sw}/d_h, Y_{sw}/d_h and d_j/d_h of multi V-shaped protrusion ribs per unit driving energy determined with

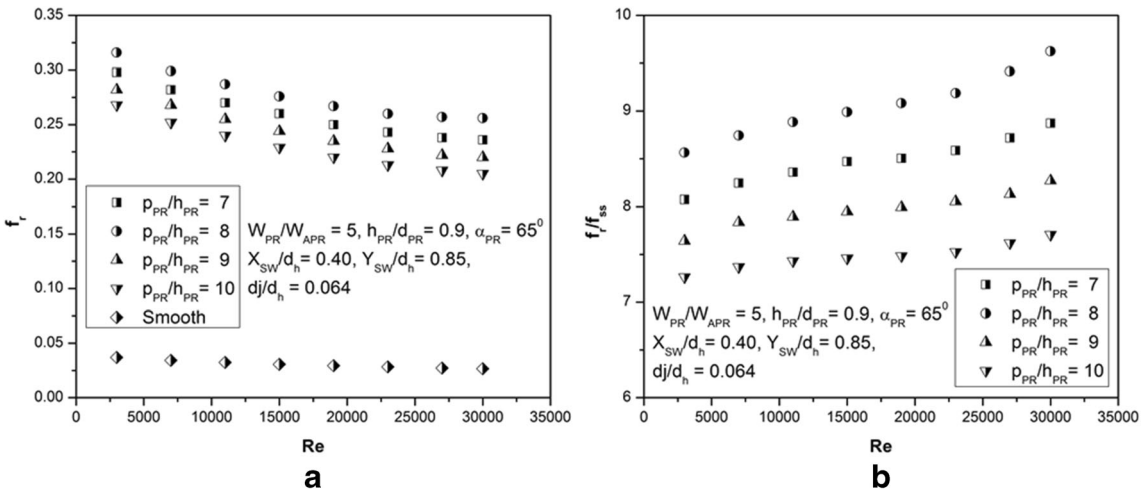

Fig. 12 **a** Effect of P_{PR}/h_{PR} on f_r **b** Effect of h_{PR}/d_{PR} on f_r/f_{ss} at selected *Re*

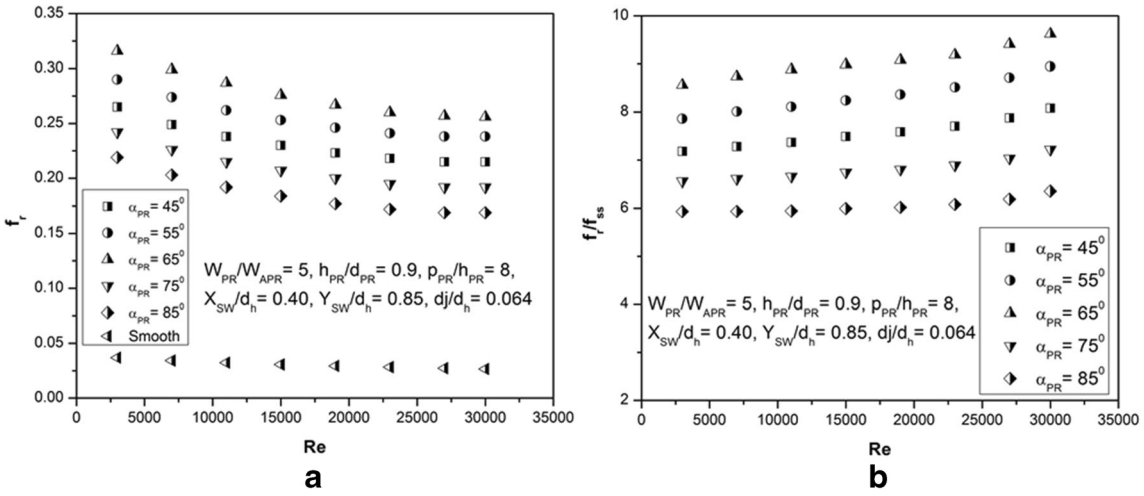

Fig. 13 **a** Effect of α_{PR} on f_r **b** Effect of α_{PR} on f_r/f_{ss} at selected *Re*

Nu for the completely formed turbulent flow in STC by flat surfaces and is specified by Eq. (26) as below:

$$\eta_{PR} = (Nu/Nu_{ss})/(f_r/f_{ss})^{0.33} \tag{26}$$

Figure 14a–d presents the influence of multi V-shaped protrusion ribs factors on η_{PR} parameters $(Nu/Nu_{ss})/(f_r/f_{ss})^{0.33}$ as a function of *Re*. Figure 14a shows the effect of η_{PR} with *Re* on W_{PR}/W_{APR} for a fixed value h_{PR}/d_{PR} = 0.9, P_{PR}/h_{PR} = 8,

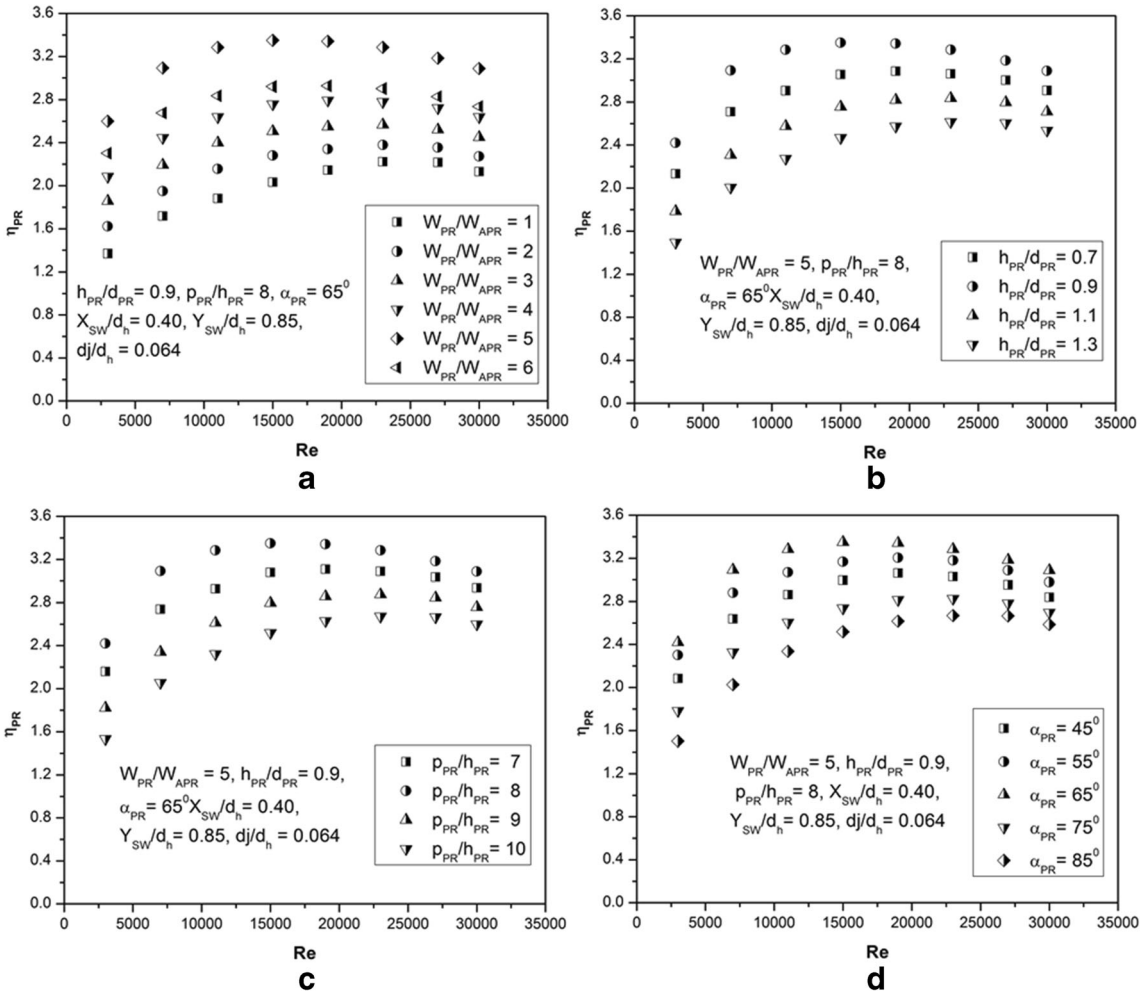

Fig. 14 Variation of multi V-shaped protrusion ribs on η_{PR} parameters **a** W_{PR}/W_{APR} **b** h_{PR}/d_{PR} **c** P_{PR}/h_{PR} **d** α_{PR}

α_{PR} = 65^0, X_{sw}/d_h = 0.40, Y_{sw}/d_h = 0.85 and d_j/d_h = 0.064. Variation of $\eta_{PR}$with respect to Re has also been plotted in Fig. 14a to show the augmentation in η_{PR} by providing multi V-shaped protrusion ribs on the beneath of the absorber plate. The maximum $\eta_{PR}$of multi V-shaped protrusion ribs collector has been found to rise from 2.60 to 3.44 with a raise in *Re* from 2500 to 35,000 for W_{PR}/W_{APR}value of 5. As the *Re* increases the turbulence decreases which leads to augment in heat transfer. Figure 14a shows that η_{PR} rises with the increase in W_{PR}/W_{APR} and receiving an utmost value at W_{PR}/W_{APR} of 5. With further increase in W_{PR}/W_{APR}, η_{PR} starts decreasing. This is because of the fact that multi V-shaped protrusion ribs creates a strong secondary stream jet close to the limbs and when the disruption from the area of the V-shaped protrusion ribs goes out and combines with the mainstream, the disturbance conducts the turbulence mixing. With the increase in number of ribs (W_{PR}/W_{APR}), it would increase number of secondary stream which improves heat transfer. By further increase in rib (beyond 5), it may outcome in the stream separation from top of rib surfaces hence drop in heat transfer. The influence of h_{PR}/d_{PR} on the η_{PR} at distinct Re is shown by the Fig. 14b. The η_{PR} rises with rise in value of h_{PR}/d_{PR} for every value of Re, which causes the highest turbulence and attaining utmost value 0.9 and then reduces for the entire Re. This is because of the fact as we raise the h_{PR}/d_{PR} height beyond the 0.9, the flows experience the high resistance which leads to large pressure drop and lesser η_{PR}. Figure 14c presents the consequence of P_{PR}/h_{PR} on η_{PR} at fixed parameters of W_{PR}/W_{APR} = 5, h_{PR}/d_{PR} = 0.9, α_{PR} = 65^0, X_{sw}/d_h = 0.40, Y_{sw}/d_h = 0.85, d_j/d_h = 0.064 and selected Re. It can be seen that the η_{PR} increases with P_{PR}/h_{PR} from 7 to 8, attains a utmost at a P_{PR}/h_{PR} of 8, and therefore it reduces with an increase in the P_{PR}/h_{PR} for all Re. It may be due to fact that stream separation may occur downstream of a multi V-shaped protrusion ribs, and reattachment of free shear layer may occur and mix with main stream, if relative pitch equal to 8 utmost η_{PR} occurs. Figure 14d shows the variation of η_{PR} with α_{PR} for distinct values of Re and fixed values of other parameters as W_{PR}/W_{APR} = 5, P_{PR}/h_{PR} = 8, h_{PR}/d_{PR} = 0.9, X_{sw}/d_h = 0.40, Y_{sw}/d_h = 0.85 and d_j/d_h = 0.064. When α_{PR} increases from 30 to 65° beyond which it again impedes. This is due to fact that an increase in α_{PR} the region developed as a outcome of multi V-shaped protrusion ribs insertion gets enriched with secondary flow streams which adds up to heat transfer from the plate to the air flowing beneath and hence increase η_{PR}. Beyond α_{PR} 65° the flow again becomes skinny and thus lesser the η_{PR}. From the η_{PR} plots, it can be seen that the value of η_{PR} increases with the *Re* initially up to a certain range of the *Re* after which it starts decreasing further. This value of the *Re* is an optimum value for the operation of STC at which the system is the most efficient. The physical mechanism of the thermo-hydraulic parameter is that its value for any system suggests the thermo-hydraulic performance equal to the times multiplied by the thermo-hydraulic performance of the conventional STC. This means that if the value of η_{PR} is less than 1 (one), the modification carried out inside the STC for enhancement of the performance has led to decrease in the performance than that of the conventional STC too. This can be due to low thermal enhancement parameter of increased value of friction factor in the STC. However, in the present study, an appreciable value of the η_{PR} has been obtained about 3.44 which show that the modification in the form of multi V-shaped protrusion ribs can augment the performance of the STC to a marginal value. Table 4 shows the values of roughness profiles parameters with which η_{PR} parameters $(Nu/Nu_{ss})/(f_r/f_{ss})^{0.33}$ has been obtained to be maximum. The highest data of $(Nu/Nu_{ss})/(f_r/f_{ss})^{0.33}$ has been attained to be 3.44 consistent to W_{PR}/W_{APR} = 5, h_{PR}/d_{PR} = 0.9, P_{PR}/h_{PR} = 8, α_{PR} = 65^0, X_{sw}/d_h = 0.40, Y_{sw}/d_h = 0.85 and d_j/d_h = 0.064 for complete values of *Re* selected for present investigation. The best results of η_{PR} parameter for different experimental factors are represented in Table 4.

8 Conclusions

This article presents experimental analysis carried out to find out *Nu* and f_r characteristics of a multi V-shaped protrusion ribs absorber plate of an impingement jet STC. The effects of various control parameters such as W_{PR}/W_{APR}, h_{PR}/d_{PR}, P_{PR}/h_{PR} and α_{PR} on *Nu* and f_r characteristics of STC are studied and the main conclusions of the study are listed below:

1. The multi V-shaped protrusion ribs on the absorber surface assist in generating vortices and creating shear layer instability which tends to increase the heat transfer to the air flowing underneath.

Table 4 Ideal values of η_{PR}

Sr. No.	Roughness parameters	Constant parameters	Ideal values of $(Nu/Nu_{ss})/(f_r/f_{ss})^{0.33}$
1	W_{PR}/W_{APR}	h_{PR}/d_{PR} = 0.9, P_{PR}/h_{PR} = 8, α_{PR} = 65^o, X_{sw}/d_h = 0.40, Y_{sw}/d_h = 0.85 and d_j/d_h = 0.064.	5
2	h_{PR}/d_{PR}	W_{PR}/W_{APR} = 5, P_{PR}/h_{PR} = 8,α_{PR} = 65^o, X_{sw}/d_h = 0.40, Y_{sw}/d_h = 0.85 and d_j/d_h = 0.064.	0.9
3	P_{PR}/h_{PR}	W_{PR}/W_{APR} = 5, h_{PR}/d_{PR} = 0.9, α_{PR} = 65^o, X_{sw}/d_h = 0.40, Y_{sw}/d_h = 0.85 and d_j/d_h = 0.064.	8
4	α_{PR}	W_{PR}/W_{APR} = 5, h_{PR}/d_{PR} = 0.9, P_{PR}/h_{PR} = 8, X_{sw}/d_h = 0.40, Y_{sw}/d_h = 0.85 and d_j/d_h = 0.064.	65^0

2. The highest value of Nu was obtained at $W_{PR}/W_{APR} = 5$, $h_{PR}/d_{PR} = 0.9$, $P_{PR}/h_{PR} = 8$, $\alpha_{PR} = 65^0$, $X_{sw}/d_h = 0.40$, $Y_{sw}/d_h = 0.85$ and $d_j/d_h = 0.064$.
3. The thermal enhancement factor achieve a better value which shows that the present modification in the solar collector channel helps is accelerating the heat transfer, however at some cost of increased friction factor. This has been evaluated in terms of thermo-hydraulic performance parameter.
4. The η_{PR} of an impinging jet, STC attached with multi V-shaped protrusion ribs on the absorbent plate is higher than the conventional STC. The highest value of the η_{PR} is found to be 3.44 for the range of parameters experimentally analyzed.

Compliance with ethical standards

Conflict of interest The authors declare that they have no conflict of interest.

References

1. Bansal NL (1999) Solar thermal collector applications in India. Renew Energy 16:618–623
2. Chauhan R, Kim SC (2019) Thermo-hydraulic characterization and design optimization of dimpled/protruded absorbers in solar heat collectors. Appl Therm Eng 154:217–227
3. Bhatti MS, Shah RK (1987) Turbulent and transition flow convective heat transfer hand book of single-phase convective heat transfer. Wiley, New York
4. Nadda R, Kumar A, Maithani R (2018) Efficiency improvement of solar photovoltaic/solar air collectors by using impingement jets: a review. Renew Sust Energ Rev 93:331–353
5. Layek A, Saini JS, Solanki SC (2007) Heat transfer and friction characteristics for artificially roughened ducts with compound turbulators. Int J Heat Mass Transf 50:4845–4854
6. Zuckerman N, Lior N (2006) Jet impingement heat transfer: physics, correlations, and numerical modeling. Adv Heat Transf 39: 565–631
7. Roger M, Buck R, Steinhagen HM (2005) Numerical and experimental investigation of multiple air jet cooling systems for application in the solar thermal receiver. ASME J Heat Transf 127:682–876
8. Han JC (2004) Recent studies in turbine blade cooling. Int J Rotat Mach 10:443–457
9. Kumar R, Kumar A, Chauhan R, Maithani R (2018) Comparative study of effect of various blockage arrangements on thermal hydraulic performance in a roughened air passage. Renew Sust Energ Rev 81:447–463
10. Chauhan R, Singh T, Kumar N, Patnaik A, Thakur NS (2017) Experimental investigation and optimization of the impinging jet solar thermal collector by Taguchi method. Appl Thermal Eng 116: 100–109
11. Singh D, Premachandran B, Kohli S (2017) Double circular air jet impingement cooling of a heated circular cylinder. Int J Heat Mass Transf 109:619–646
12. Babic DM, Murray DB, Torrance AA (2005) Mist jet cooling of grinding processes. Int J Mach Tools Manuf 45:1171–1177
13. Nadda R, Kumar A, Maithani R (2017) Developing heat transfer and friction loss in an impingement jets solar air heater with multiple arc protrusion obstacles. Sol Energy 158:117–131
14. Chauhan R, Thakur NS, Singh T, Sethi M (2018) Exergy based modeling and optimization of solar thermal collector provided with impinging air jets. J King Saud Univ–Eng Sci 30:355–362
15. Chauhan R, Singh T, Thakur NS, Kumar N, Kumar R, Kumar A (2018) Heat transfer augmentation in solar thermal collectors using impinging air jets: a comprehensive review. Renew Sust Energ Rev 82:3179–3190
16. Matheswaran MM, Arjunan TV, Somasundaram D (2018) Analytical investigation of solar air heater with jet impingement using energy and exergy analysis. Sol Energy 161:25–37
17. Aboghrara AM, Baharudin BTHT, Alghoul MA, Sopian K, Adam NM, Hairuddin AA (2017) Performance analysis of single pass solar air heater with jet impingement on wavy shape corrugated absorber plate. Case Studies in Thermal Engineering 10:111–120
18. Brideau SA, Collins MR (2012) Experimental model validation of a hybrid PV/thermal air based collector with impinging jets. Energy Proced 30:44–54
19. Chauhan R, Thakur NS (2013) Heat transfer and friction factor correlations for impinging jet solar air heater. Exp Thermal Fluid Sci 44:760–767
20. Guo Q, Wen Z, Dou R (2017) Experimental and numerical study on the transient heat-transfer characteristics of circular air-jet impingement on a flat plate. Int J Heat Mass Transf 104:1177–1188
21. Nadda R, Maithani R, Kumar A (2017) Effect of multiple arc protrusion ribs on heat transfer and fluid flow of a circular-jet impingement solar air passage. Chem Eng Process Process Intensif 120: 114–133
22. Rajaseenivasan T, Prasanth SR, Antony MS, Srithar K (2016) Experimental investigation on the performance of an impinging jet solar air heater. Alexand Eng J 56:63–69
23. Nadda R, Kumar A, Maithani R, Kumar R (2017) Investigation of thermal and hydrodynamic performance of impingement jets solar air passage with protrusion with combination arc obstacle on the heated plate. Exp Heat Transfer 31:232–250
24. Mishra PK, Nadda R, Kumar R, Rana A, Sethi M, Ekileski A (2018) Optimization of multiple arcs protrusion obstacle parameters using AHP-TOPSIS approach in an impingement jet solar air passage. Heat Mass Transf 54:3797–3808
25. Geers LFG, Tummers MJ, Hanjalic K (2004) Experimental investigation of impinging jet arrays. Exp Fluids 36:946–958
26. Kercher DM, Tabakoff W (2016) Heat transfer by a spare Array of round air jets impinging perpendicular to a flat surface including the elect of spent air. J Eng Power 1970:73–82
27. Metzger DE, Florschuetz LW, Takeuchi DI, Behee RD, Berry RA (1979) Heat transfer characteristics for inline and staggered arrays of circular jets with cross flow of spent air. J Heat Trans 101:526–531
28. Brideau SA, Collins MR (2014) Development and validation of a hybrid PV/thermal air based collector model with impinging jets. Sol Energy 102:234–246
29. Nadda R, Kumar R, Kumar A, Maithani R (2018) Optimization of single arc protrusion ribs parameters in solar air heater with impinging air jets based upon PSI approach. Therm Sci Eng Prog 7:146–154
30. Goodro M, Park J, Ligrani P, Fox M, Moon HK (2007) Effects of Mach number and Reynolds number on jet array impingement heat transfer. Int J Heat Mass Trans 50:367–380
31. Goodro M, Park J, Ligran P, Fox M, Moon HK (2008) Effects of hole spacing on spatially-resolved jet array impingement heat transfer. Int J Heat Mass Trans 51:6243–6253
32. Lee J, Ren Z, Ligrani P, Lee DH, Fox MD, Moon HK (2014) Cross-flow effects on impingement array heat transfer with varying jet-to-

target plate distance and hole spacing. Int J Heat Mass Trans 75: 534–544
33. Nayak RK, Singh SN (2016) Effect of geometrical aspects on the performance of jet plate solar air heater. Sol Energy 137:434–440
34. Soni A, Singh SN (2017) Experimental analysis of geometrical parameters on the performance of an inline jet plate solar air heater. Sol Energy 148:149–156
35. Yu P, Zhu K, Shi Q, Yuan N, Ding J (2017) Transient heat transfer characteristics of small jet impingement on a high-temperature flat plate. Int J Heat Mass Trans 114:981–991
36. Zukowski M (2015) Experimental investigations of thermal and flow characteristics of a novel micro jet air solar heater. Appl Energy 142:10–20
37. Kumar R, Sethi M, Chauhan R, Kumar A (2017) Experimental study of enhancement of heat transfer and pressure drop in a solar air channel with discretized broken V-pattern baffle. Renew Energy 101:856–872
38. Kline SJ, Mcclintock FA (1953) Describing uncertainties in single sample experiments. Mech Eng 75:3–8
39. Lewis MJ (1975) Optimizing the thermohydraulic performance of rough surfaces. Int J Heat Mass Transf 18:1243–1248